Structure-Composition-Property Relationships of 6H-BaTi$_{1-y}$Co$_y$O$_{3-\delta}$ (0.1 ≤ y ≤ 0.4)

Laura Miranda,[†,‡] Khalid Boulahya,[†] María Hernando,[†] Derek C. Sinclair,[‡]
Félix Jiménez-Villacorta,[§] Aurea Varela,[†] Jose M. González-Calbet,[†] and Marina Parras*,[†]

[†]*Departamento de Química Inorgánica, Facultad de Químicas, Universidad Complutense de Madrid, E-28040-Madrid, Spain,* [‡]*Department of Material Science and Engineering, University of Sheffield, Mappin Street, Sheffield S1 3JD, U.K., and* [§]*SpLine, Spanish CRG beamline at the ESRF 6 rue Jules Horowitz - B.P.220, F-38043 Grenoble CEDEX, France and Instituto de Ciencia de Materiales de Madrid- CSIC, Cantoblanco 28049, Spain*

A solid solution of 6H-type BaTi$_{1-y}$Co$_y$O$_{3-\delta}$ samples where 0.1 ≤ y ≤ 0.4 and δ ≤ 0.05 has been prepared in air and characterized by a combination of X-ray, neutron, and electron diffraction, X-ray absorption spectroscopy, hydrogen-reduction thermogravimetric analysis, high resolution electron microscopy, magnetic susceptibility measurements, and impedance spectroscopy. For y = 0.1, Co acts as an acceptor dopant and is incorporated as Co^{III} ions with charge balanced achieved by the formation of O(2) oxygen vacancies in the *h*-BaO$_3$ layers that separate pairs of face-sharing octahedra. For samples with y > 0.1, Co is present as both Co^{III} and Co^{IV} ions and in all cases δ ~ 0.03. This indicates a change from primarily aliovalent (Co^{III}) to isovalent (Co^{IV}) doping with increasing Co-content with a general formula BaTi$^{IV}_{1-y}$(Co$^{III}_{0.06}$Co$^{IV}_{y-0.06}$)O$_{2.97}$ for 0.2 ≤ y ≤ 0.4. All samples are semiconducting at room temperature with relative permittivity in the range ~20–50. The bulk conductivity increases with y and displays complex, non-Arrhenius-type behavior. All samples show paramagnetic behavior that can be fitted to the Curie–Weiss law from ~150 to 300 K with a negative Weiss temperature indicating antiferromagnetic interactions between the magnetic Co ions. X-ray absorption spectroscopy data on a sample of y = 0.1 that retained the 6H-structure after heat treatment under reducing conditions revealed the existence of mixed state Co^{II} and Co^{III} ions. A solid solution volume therefore exists for 6H–Ba(Ti,Co)O$_{3-\delta}$ where the oxidation state of Co can vary from II to IV depending on the preparative conditions.

Introduction

The tetragonal polymorph of BaTiO$_3$ is ferroelectric and is extensively used as a commercial electroceramic in several applications including multilayer capacitors, positive temperature coefficient of resistance (ptcr) thermistors, and piezoelectric transducers/actuators.[1] BaTiO$_3$ exhibits a variety of polymorphic forms, most of which are based on 100% cubic close packed (ccp) BaO$_3$ layers (so-called 3C-type perovskite) with Ti ions in octahedral sites that form a 3D network of corner-sharing TiO$_3$ units. Above ~1733 K in air, the BaO$_3$ close packing changes to a mixed (66.7%) cubic- and (33.3%) hexagonal-type arrangement (6H-type perovskite), and this results in a different arrangement of the TiO$_6$ octahedra whereby they form a sequence of face sharing Ti$_2$O$_9$ dimers connected via a single corner sharing TiO$_6$ unit along the hexagonal *c* axis, Figure 1. On cooling in air below ~1733 K, the 6H-type structure reverts to the 3C-type structure, and the ideal cubic perovskite cell undergoes a series of distortions at lower temperatures, *viz.* tetragonal (below ~403 K),

orthorhombic (below ~278 K), and rhombohedral (below ~183 K). The hexagonal polymorph can be stabilized at room temperature if samples are processed at elevated temperature under inert or reducing conditions to induce oxygen deficiency, δ. The crystal symmetry at room temperature changes from tetragonal- to cubic-perovskite for δ < 0.03 before transforming to the hexagonal 6H-type perovskite for δ > 0.03. The upper limit of oxygen deficiency in undoped BaTiO$_3$ is δ ~ 0.17, corresponding to a formula of BaTi$^{4+}_{0.66}$Ti$^{3+}_{0.34}$O$_{2.83}$.[2]

In recent years, the electrical properties of the 6H polytype have received attention due to the attractive microwave dielectric resonator properties reported for other related hexagonal polytypes.[3,4] Substitution of ~5 at% Ti by other transition metal cations such as Fe, Mn, Co, or Ni, in BaTiO$_3$, is effective in suppressing the 6H- to 3C-type polymorphic phase transition such that the 6H structure is stable at room temperature.[5] Although these materials have been reported to have high permittivity

(1) Sinclair, D. C.; West, A. R. *J. Appl. Phys. C* **1989,** *66,* 3850.

(2) Sinclair, D. C.; Skakle, J. M. S.; Morrison, F. D.; Smith, R. I; Beales, T. P. *J. Mater. Chem.* **1999,** *9,* 1327.
(3) Feteira, A.; Sarma, K.; Alford, N. M.; Reaney, I. M.; Sinclair, D. C. *J. Am. Ceram. Soc.* **2003,** *86,* 511.
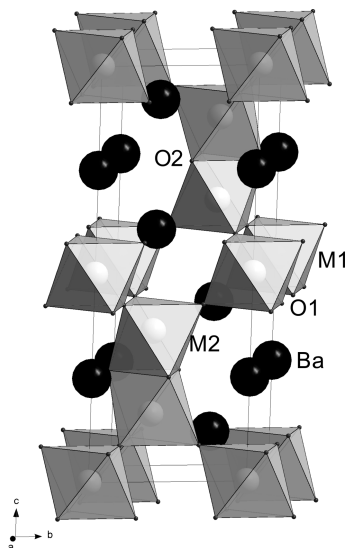(4) Vineis, C.; Davies, P. K.; Negas, T.; Bell, S. *Mater. Res. Bull.* **1996,** *31,* 431.

Article

Chem. Mater., Vol. 23, No. 4, 2011   1051

Figure 1. Structural model for the 6H polytype.

values ($\varepsilon \sim 50$) the introduction of cations with electrons in their d orbitals results in an increase in bulk conductivity and, therefore, to high dielectric losses. This currently prohibits their possible use as high permittivity microwave dielectric resonator materials; however, a better understanding of the influence of transition metal doping on the structure-composition-property relationships of 6H-Ba-TiO$_3$ is required to improve our knowledge of the defect chemistry in this important electroceramic and also to shed light on how other perovskite-based hexagonal materials may be developed. There is also a need to rationalize the relative importance of factors such as the presence of oxygen vacancies and transition metal cations with partially filled d-shells on the Ti-site(s) that seem to favor the formation of the 6H-polymorph over the 3C-polymoprh for BaTiO$_3$.

Recent work on the BaTi$_{1-y}$Mn$_y$O$_{3-\delta}$ system[6,7] shows the 6H polytype is retained between $0 \leq y \leq 0.5$ and $0 \leq \delta \leq 0.15$. The bulk conductivity increases with the Mn content, and none of the materials follow the Arrhenius law over the measured temperature range. Instead, variable range hopping (VRH) conduction is observed at low temperatures, whereas near room temperature (RT) a band gap-type model can be applied. In general, the charge compensation mechanism involves the creation of oxygen vacancies. The presence of acceptor dopants, i.e., cations with lower oxidation state than Ti, introduces acceptor-states within the band gap, and these can accept electrons from the valence band thus giving rise to p-type semiconductivity. Although this explanation is generally acceptable for 6H-BaTi$_{1-y}$M$_y$O$_{3-\delta}$ systems, it can be very difficult to reach a complete understanding of the role(s) of the dopant on the electrical properties, especially when

the dopant ion may exhibit more than one oxidation state. In addition, these materials are often studied in the form of ceramics, and it is difficult to ensure complete solid−gas equilibrium between the material and the processing ambient is maintained from the high sintering temperatures down to room temperature, RT. This can easily result in oxygen concentration gradients within individual grains and thus lead to changes in the oxidation state(s) and distribution of the dopant ion between the inner and outer regions of the grains. Such experimental complexities make it difficult to establish the conduction mechanism(s) as more than one mechanism may be present.

The purpose of this paper is to report the structure-composition-property relationships of 6H-BaTi$_{1-y}$Co$_y$O$_{3-\delta}$ for $0 \leq y \leq 0.4$. A comprehensive physical study has been undertaken in an attempt to improve our understanding of the role of Co as a dopant in BaTiO$_3$ and, in particular, in the stabilization and electrical properties of the 6H polymorph.

Experimental Section

Polycrystalline samples of BaTi$_{1-y}$Co$_y$O$_{3-\delta}$ ($0.1 \leq y < 0.5$) were prepared by heating well-ground, stoichiometric mixtures of BaCO$_3$ (Aldrich 99.9%), TiO$_2$ (Aldrich 99.9%), and Co$_3$O$_4$ (Aldrich 99.9%). All samples were placed in Pt crucibles and subsequently air-quenched after all treatments. The mixtures were fired at 1123 K in air for 24 h. The samples were then heated in air at different temperatures depending on the Co content; *viz.* 2 days at 1648 K for y = 0.1 sample (BaTi$_{0.9}$Co$_{0.1}$O$_{2.95}$); 3 days at 1473 K for y = 0.2; 3 days at 1373 K for y = 0.3; and 6 days at 1398 K for y = 0.4 sample. In addition, another y = 0.1 sample (labeled as the green phase) was obtained from a reduction process of BaTi$_{0.9}$Co$_{0.1}$O$_{2.95}$ (see below).

The average cationic composition was determined by X-Ray Fluorescence (XRF). The overall oxygen content was determined by thermogravimetric analysis on a thermobalance based on a CAHN D-200 electrobalance which allows determination of the oxygen content within $\pm 1 \times 10^{-3}$ on a sample of about 100 mg working under 0.5 bar/reducing atmosphere and confirmed by neutron diffraction and XANES (X-ray Absorption Near Edge Structure) results.

Powder X-ray diffraction (XRD) patterns were collected using CuK$_\alpha$ monochromatic radiation (λ = 1.54056 Å) at RT on a Panalytical X′PERT PRO MPD diffractometer equipped with a germanium 111 primary beam monochromator and X′Celerator fast detector. Neutron diffraction (ND) data were collected at RT on the high resolution powder diffractometer D2B at the Institute Laue Langevin (ILL), Grenoble (France) with neutrons of wavelength 1.594 Å. The angular range covered by the detectors extends from 0 to 160° with a step size of 0.05°. Diffraction data were analyzed by the Rietveld method[8] using the Fullprof program.[9]

To establish the oxidation state(s) of Ti and Co ions, X-ray absorption spectroscopy measurements at the Co K-edge and the Ti K-edge have been performed on the Spanish CRG beamline (SpLine) at the European Synchrotron Radiation Facility. XANES spectra have been collected in the fluorescence yield mode using a 13-element Si(Li) detector due to the large absorption coefficient of the Ba cation at these energies. A Co foil, BaCoO$_3$ and

(5) Keith, G. M.; Rampling, M. J.; Sarma, K.; Alford, N. Mc.; Sinclair, D. C. *J. Eur. Ceram. Soc.* **2004**, *24*, 1721.
(6) Miranda, L.; Sinclair, D. C.; Hernando, M.; Varela, A.; Ramírez, J.; Boulahya., K.; González-Calbet, J. M.; Parras, M. *Chem. Mater.* **2010**, *22*, 4320.
(7) Miranda, L.; Feteira, A.; Sinclair, D. C.; Boulahya; Hernando, M.; Ramírez, J.; Varela, A.; González-Calbet, J. M.; Parras, M. *Chem. Mater.* **2009**, *21*, 1731.

(8) Rietveld, H. M. *J. Appl. Crystallogr.* **1969**, *2*, 65.
(9) Rodríguez- Carvajal *J. Physica B* **1993**, *192*, 55.

Co_3O_4 were used as Co-references. Several scans per sample were obtained to improve the signal-to-noise ratio. Data treatment of the experimental XANES spectra has been performed with the ATHENA software.[10]

Selected area electron diffraction (SAED) and high resolution electron microscopy (HREM) were performed using a JEOL 3000 FEG electron microscope, fitted with a double tilting goniometer stage ($\pm 22°$, $\pm 22°$). Simulated HREM images were calculated by the multislice method using the MacTempas software package.

DC magnetization was measured in a SQUID magnetometer, in the range ~ 2 to 300 K under an applied magnetic field of 1000 Oe.

Powder was milled using a mortar and pestle and uniaxially pressed (Specac, Kent, UK) into cylindrical (length ~ 5 mm) pellets under an applied pressure of 50 MPa and then isostatically pressed (model CIP 32330, Flow Autoclave System Inc., Columbus, OH) at 200 MPa. Pellets were sintered in air at the synthesis temperature for 2 h and then quenched in air reaching a ceramic density of 4.63 g.cm^{-3} (93% of the theoretical X-ray density), 4.02 g.cm^{-3} (75%), 5.34 g.cm^{-3} (89%), and 5.23 g.cm^{-3} (87%) for $BaTi_{0.9}Co_{0.1}O_{2.95}$ ($y = 0.1$), $y = 0.2$, $y = 0.3$, and $y = 0.4$ samples, respectively. Electrodes fabricated from gold paste (T-10112, Engelhard-CLAL, Cinderford, Gloucestershire, UK) were applied to both major faces of the pellets, which were sintered in air at 1073 K for 1 h to remove volatiles and harden the residue. The electrical properties of the ceramics were investigated in the temperature range $10-300$ K using a cryocooler coupled to an LCR bridge (model E4980A, Agilent, Palo Alto, CA) and to an impedance analyzer (model HP 4192A, Hewlett-Packard, Palo Alto, CA) for fixed frequency capacitance and Impedance Spectroscopy (IS) measurements, respectively. The temperature range $300-670$ K was measured for $BaTi_{0.9}Co_{0.1}O_{2.95}$ using a ceramic jig in a high temperature furnace coupled to an impedance analyzer (model HP 4192A, Hewlett-Packard, Palo Alto, CA). All impedance data were corrected for sample geometry and analyzed using the commercial software package Z-view (Scribner Associates, Inc., Charlottesville, VA, version 2.1).

Results and Discussion

The overall oxygen content was determined by hydrogen reduction thermogravimetric analysis and confirmed by neutron diffraction and XANES results. Samples were reduced under 0.3 bar H_2/0.2 bar He atmosphere and heated at 6 °C/min up to 700 °C. The annealing temperature was kept constant for several hours to ensure a constant weight was obtained. Ba_2TiO_4, $BaTiO_3$, and Co metal were identified by XRD as the final products of the reduction for $y \geq 0.2$ samples; their stoichiometric relationship is dependent on the Ti/Co ratio of the sample, according to the following reaction

$$BaTi_{1-y}Co_yO_{3-\delta} \xrightarrow{H_2} yBa_2TiO_4 + (1-2y)BaTiO_3$$
$$+ yCo + (2y\text{-}\delta)H_2O$$
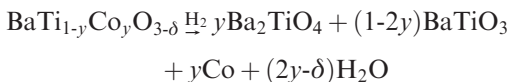
From the weight loss, the oxygen contents correspond to $BaTi_{0.8}Co_{0.2}O_{2.97(1)}$, $BaTi_{0.7}Co_{0.3}O_{2.97(1)}$, and $BaTi_{0.6}Co_{0.4}O_{2.97(1)}$ (Figure 1 of the Supporting Information). However, the $y = 0.1$ sample follows a different reduction pathway as shown in Figure 2 of the Supporting Information. The thermogravimetric reduction curve shows an abrupt weight loss at temperature close to 300 °C, followed
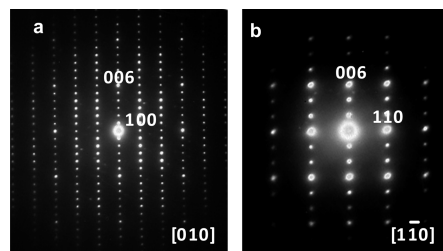

Figure 2. SAED patterns along [010] (a) and [1$\bar{1}$0] (b) for 6H-$BaTi_{0.9}$-$Co_{0.1}O_{2.95}$.

by a weight increase when the sample is cooled down. Constant weight is attained at room temperature after several hours. The green final product was identified by XRD as single-phase 6H-type that, according to thermogravimetric results, corresponds to $BaTi_{0.9}Co_{0.1}O_{2.92(1)}$.

The green phase was stabilized from the reduction process of the $BaTi_{0.9}Co_{0.1}O_{2.95}$ sample described above. We were unable to perform a synthesis procedure to obtain larger amounts of this compound as a single-phase to facilitate in-depth structural and physical characterization. Nevertheless, it has been characterized by XRD, HREM/SAED, XANES, and magnetic measurements.

The XRD patterns of all the stabilized phases can be indexed on the basis of a 6H$-$(hcc)$_2$ hexagonal unit cell, isotypic with the 6H-$BaTiO_3$ structure [Figure 1]. The pattern for $BaTi_{1/2}Co_{1/2}O_{3-\delta}$ showed evidence of both 5H and 6H polytypes. It was not possible to eliminate the 5H polytype using a variety of processing conditions, therefore suggesting the solid solution limit to be ~ 0.40.

Microstructural characterization of $BaTi_{1-y}Co_yO_{3-\delta}$, $0.1 \leq y \leq 0.4$, samples, studied by SAED and HREM, confirms the XRD results. Selected area electron diffraction (SAED) was used to fully reconstruct the reciprocal space, confirming all phases belong to the same 6H polytype structure. As an example, the most relevant zone axes, [010] and [1$\bar{1}$0], corresponding to $BaTi_{0.9}Co_{0.1}O_{2.95}$, are shown in Figure 2. All maxima can be indexed on the basis of a hexagonal lattice with cell parameters $a = 5.7$ and $c = 14.0$ Å; the reflection conditions are compatible with the $P6_3/mmc$ (N°196) space group, previously proposed for 6H- $BaTiO_3$.[11]

The HREM micrograph corresponding to $BaTi_{0.9}$-$Co_{0.1}O_{2.95}$ along [010] (Figure 3) shows an apparently well ordered material with d-spacings of 4.9 and 14.0 Å, corresponding to d_{100} and d_{001}, respectively. The structure can be directly revealed from the contrast observed in this image: the bright dots correspond to rows of Ba and Ti/Co atoms. From the Ba distribution this contrast can be interpreted as an (hcc)$_2$ stacking sequence. From the refined atomic parameters of $BaTi_{0.9}Co_{0.1}O_{2.95}$ (see the next section), an image calculation was performed. The Simulated image (inset in Figure 3) gives a good fit to the experimental image at $\Delta t = 30$ Å and $\Delta f = -450$ Å.

A ND study performed at RT was used for accurate structural characterization to locate the oxygen vacancies revealed by TGA measurements. In addition, the

(10) Ravel, B.; Newville, M. *J. Synchrotron Radiat.* **2005**, *12*, 537.

(11) Burbank, R. D.; Evans, H. T. *Acta Crystallogr.* **1948**, *1*, 330.

large contrast between the scattering lengths of Ti (-3.44 fm) and Co (2.49 fm) makes ND a suitable tool to get information on the possible presence of cationic order in these samples. ND data were satisfactorily fitted using the atomic positions corresponding to the 6H-BaTiO$_3$[11] polytype in the P6$_3$/*mmc* space group. Initially, Co and Ti were distributed randomly over the two distinct metal-sites according to the Co:Ti ratio, and each of the sites was constrained to be fully occupied. The occupancy numbers of all the oxide sites were also refined. The O(1) site is fully occupied within error, whereas the O(2) site is not fully occupied, thus confirming vacancies in the oxygen sublattice (see Table 1) to be located in the hexagonal layers. The compositions obtained were also in agreement with the TGA analysis, viz. BaTi$_{0.9}$Co$_{0.1}$O$_{2.95(1)}$, BaTi$_{0.8}$Co$_{0.2}$O$_{2.97(1)}$, and BaTi$_{0.6}$Co$_{0.4}$O$_{2.97(1)}$.
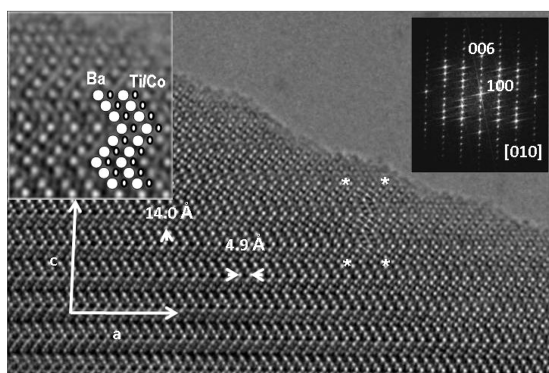

Figure 3. [010] HREM image corresponding to 6H-BaTi$_{0.9}$Co$_{0.1}$O$_{2.95}$. Inset shows the simulated image for $\Delta f = -450$ Å, $\Delta t = 30$ Å and a Fourier transform was performed on the HREM micrograph.

Fitting of the ND data and the difference between observed and calculated data for $y = 0.1$ is shown in Figure 4. The same information for $y = 0.2$ and 0.4 is included in the Supporting Information (Figure 3a,b). The refined atomic positions resulting from the refinement for the three 6H-polytypes are listed in Table 1; Table 2 lists selected interatomic distances.

The structure consists of face-sharing octahedral dimers separated by a single corner sharing octahedra, Figure 1. There are two crystallographically different octahedral sites, M(1) and M(2) corresponding to the M cations in the corner and face sharing octahedra, respectively. M(1) is a regular site with six identical M-O distances. To reduce electrostatic repulsion between metal ions in adjacent face-sharing octahedra (M(2) site), the cations are displaced from the center of the octahedron to the adjacent cubic layer. This results in a distorted octahedral environment with three longer and three shorter M(2)-O distances (see Table 2).

The distribution of Ti and Co over the two octahedral sites is given in Table 1. For all samples, the corner-shared octahedron (M(1) site) is occupied primarily by Ti, and for BaTi$_{0.9}$Co$_{0.1}$O$_{2.95(1)}$ Ti fully occupies this position. This feature has been found in other polytypes like 12R-BaMn$_{0.5}$Ti$_{0.5}$O$_3$[12] or 6H-BaMn$_{1-y}$Ti$_y$O$_{3-\delta}$.[7] The M(1)-O distances, see Table 2, are in excellent agreement with the Ti-O bond length of 1.983(5) Å in 6H-BaTiO$_3$.[11] Accordingly, ND refinements allow the following cationic distributions, Ba(Ti$_{0.33}$)$_{M1}$(Ti$_{0.57}$Co$_{0.09}$)$_{M2}$O$_{2.95}$ for $y = 0.10$, Ba(Ti$_{0.27}$Co$_{0.06}$)$_{M1}$(Ti$_{0.53}$Co$_{0.13}$)$_{M2}$O$_{2.97}$ for $y = 0.20$, and Ba(Ti$_{0.24}$Co$_{0.09}$)$_{M1}$(Ti$_{0.37}$Co$_{0.30}$)$_{M2}$O$_{2.97}$ for $y = 0.40$. These are in excellent agreement with the nominal starting compositions.

Table 1. Final Structural Parameters of the 6H-BaTi$_{1-y}$Co$_y$O$_{3-\delta}$ System ($y = 0.1, 0.2, 0.3, 0.4$)^{b,e}

	BaTi$_{0.9}$Co$_{0.10}$O$_{2.95}$	BaTi$_{0.8}$Co$_{0.2}$O$_{2.97}$	BaTi$_{0.7}$Co$_{0.3}$O$_{2.97}$^{a}	BaTi$_{0.6}$Co$_{0.4}$O$_{2.97}$
Ba(1) (0, 0, 1/4)				
Biso (Å^2)	0.50(3)	0.71(4)	0.38(2)	0.16(6)
Occ	1	1	1	1
Ba(2) (1/3, 2/3, z)				
z	0.09647(18)	0.0939(2)	0.09264(8)	0.09538(14)
Biso (Å^2)	0.58(3)	0.71(4)	0.24(2)	0.35(4)
Occ	1	1	1	1
M(1) (0, 0, 0)				
Biso (Å^2)	1.53(11)	0.34 (14)	0.10(1)	0.7(1)
Occ	1	0.817(8)/0.183(8)^c	0.60/0.40^d	0.736(3)/0.274(3) ^{c}
M(2) (1/3, 2/3, z)				
z	0.6519(4)	0.6503 (6)	0.65219(19)	0.6540(3)
Biso (Å^2)	0.39(11)	1.16 (14)	0.39(1)	0.6(1)
Occ	0.8612(10)/0.1388(10)^c	0.798(8)/0.202(8) ^{c}	0.60/0.40^d	0.565(1)/0.435(1) ^{c}
O(1) (x, 2x, z)				
x	0.8342(2)	0.8347(2)	0.8322(7)	0.8344(2)
z	0.08038(8)	0.08095 (10)	0.0824(3)	0.08074(11)
Biso (Å^2)	0.547(13)	0.80 (2)	0.30(7)	0.46(2)
Occ	1	1	1	1
O(2) (x, 2x, 1/4)				
x	0.5169(4)	0.5180 (5)	0.5119(4)	0.5186(5)
Biso (Å^2)	0.611(9)	1.01 (3)	0.30(7)	1.32(6)
Occ	0.960(6)	0.980(6)	0.971	0.971(7)
a = b (Å)	5.71833(2)	5.70446 (4)	5.70300(1)	5.69211(2)
c (Å)	13.98627(8)	13.97636 (1)	13.97725(5)	13.98032(9)
V (Å^3)	396.076(4)	393.870 (4)	393.694(2)	392.278(4)

^{a} Parameters obtained from X-ray diffraction data. ^{b} Space group P6$_3$/*mmc*. ^{c} Ti/Co ratio. Metal site occupancy. ^{d} Ti/Co ratio. Metal site occupancy cannot be refined. ^{e} Fit parameter: **BaTi$_{0.90}$Co$_{0.10}$O$_{2.95}$**: Rp = 2.31, R$_{wp}$ = 3.05, R$_B$ = 1.83, χ^2 = 1.77; **BaTi$_{0.80}$Co$_{0.20}$O$_{2.97}$**: Rp = 4.16, R$_{wp}$ = 5.68, R$_B$ = 3.62, χ^2 = 3.59; **BaTi$_{0.70}$Co$_{0.30}$O$_{2.97}$**: Rp = 6.22, R$_{wp}$ = 7.90, R$_B$ = 3.76, χ^2 = 1.63; **BaTi$_{0.60}$Co$_{0.40}$O$_{2.97}$**: R$_p$ = 5.58, R$_{wp}$ = 6.74, R$_B$ = 4.15, χ^2 = 2.14.
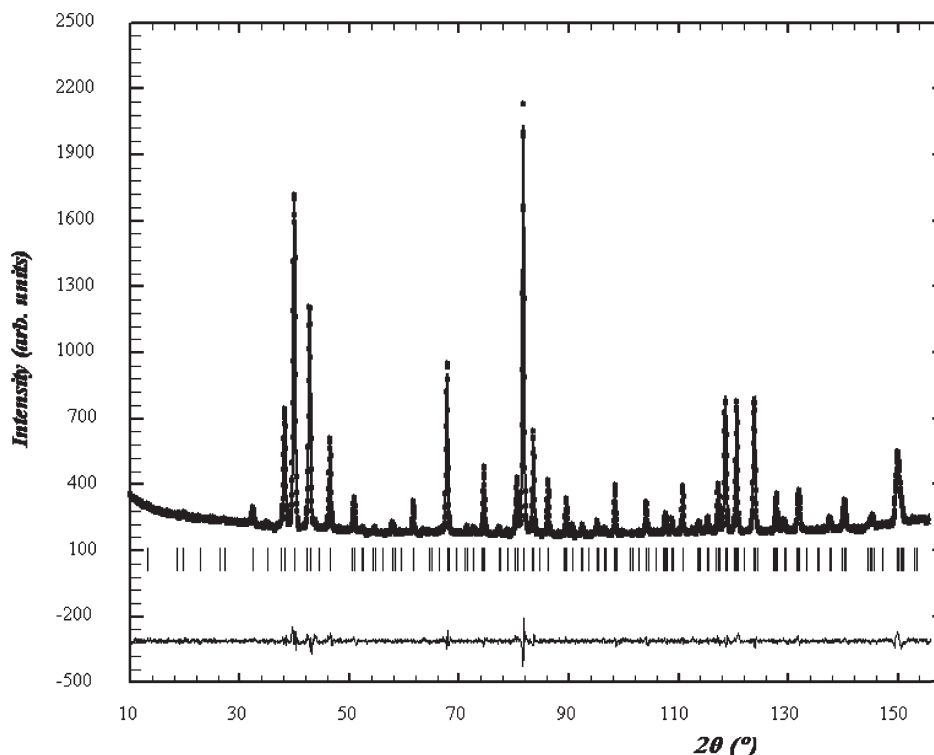
Figure 4. Observed, calculated, and difference profile of ND data for 6H-BaTi$_{0.9}$Co$_{0.1}$O$_{2.95}$ at room temperature.

Table 2. Selected Interatomic Distances (Å) and Angles for 6H-BaTi$_{0.90}$Co$_{0.10}$O$_{2.95}$, 6H-BaTi$_{0.80}$Co$_{0.20}$O$_{2.97}$, 6H-BaTi$_{0.70}$Co$_{0.30}$O$_{2.97}$, and 6H-BaTi$_{0.60}$Co$_{0.40}$O$_{2.97}$

		BaTi$_{0.9}$Co$_{0.1}$O$_{2.95}$	BaTi$_{0.80}$Co$_{0.20}$O$_{2.97}$	BaTi$_{0.70}$Co$_{0.30}$O$_{2.97}$ [a]	BaTi$_{0.60}$Co$_{0.40}$O$_{2.97}$
Ba(1)−O(1)	x6	2.8853(12)	2.8722(14)	2.869(5)	2.8760(14)
Ba(1)−O(2)	x6	2.8641(16)	2.858(3)	2.854(14)	2.864(3)
Ba(2)−O(1)	x6	2.8680(8)	2.8580(12)	2.855(4)	2.8652(8)
Ba(2)−O(1)	x3	2.985(2)	2.954(3)	2.942(3)	2.967(2)
Ba(2)−O(2)	x3	2.814(2)	2.845(3)	2.819(9)	2.833(3)
M(1)-O(1)	x6	1.9901(13)	1.9868(15)	2.018(4)	1.9902(14)
M(2)-O(1) x3		1.937(3)	1.922(5)	1.904(5)	1.9162(14)
M(2)-O(2) x3		2.019(4)	2.024 (7)	2.050(11)	2.019(2)
M(2)-M(2)		2.744(8)	2.787(14)	2.734(3)	2.775(14)
M(1)-M(2)		3.927(6)	3.906(17)	3.9200(15)	3.904(14)

[a] Distances obtained from XRD data.

Structural refinement for BaTi$_{0.7}$Co$_{0.3}$O$_{2.97}$ was performed by XRD data. A model based from ND data obtained for y = 0.1, 0.2, and 0.4 samples was refined. The oxygen deficiency obtained from TGA analysis was located on the O(2) site and was not refined (fixed). Isotropic atomic displacement parameters were refined for each atom independently and constrained to be the same for the oxygen atoms. Good agreement between observed and calculated diffraction patterns was achieved as shown in Figure 3c of the Supporting Information.

The synthesis procedure for the green phase (BaTi$_{0.9}$-Co$_{0.1}$O$_{2.92}$) produced only a very small amount of product, thus preventing adequate characterization by ND. XRD, HREM/SAED, and XANES, however, have been used to characterize this phase.

First, to confirm that 6H-BaTi$_{0.9}$Co$_{0.1}$O$_{2.92}$ retains the original symmetry and structural features of the 6H

polytype, the green sample was studied by HREM. The HREM micrograph (Figure 5a) shows an apparently well ordered material with *d*-spacings of 4.9 Å and 14.0 Å corresponding to d$_{100}$ and d$_{001}$, respectively. A SAED pattern along the [010] zone axis (Figure 5b) confirms the symmetry is retained, and no additional structural ordering is formed during the reduction process. The whole crystal appeared homogeneous and only maxima corresponding to the 6H polytype were observed. Accordingly, the structural parameters obtained from the ND results for the black y = 0.1 sample were used as a starting model in the refinement of the XRD pattern for the green phase. The structural details obtained and a graphical result of the fitting of the XRD data for 6H-BaTi$_{0.9}$Co$_{0.1}$O$_{2.92}$ at room temperature are listed in Table I and Figure 4, respectively, of the Supporting Information.

For further insight into the characterization of the 6H-BaTi$_{1-y}$Co$_y$O$_{3-\delta}$ solid solution, a XANES study was

(12) Caballero, A.; Espinós, J. P.; Fernández, A.; Leinen, D.; González-Elipe, A. R. *Nucl. Instrum. Methods* **1995**, *B 97*, 397.
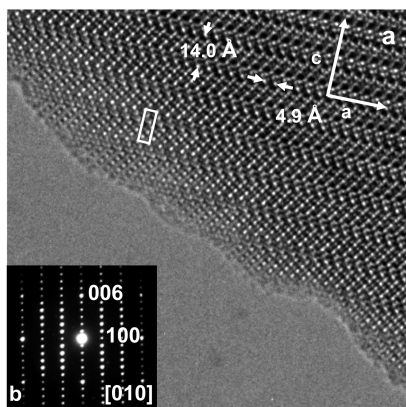
Figure 5. (a) SAED patterns and (b) corresponding HREM image along [010] zone axis for an ordered crystal of 6H-BaTi$_{0.9}$Co$_{0.1}$O$_{2.92}$.
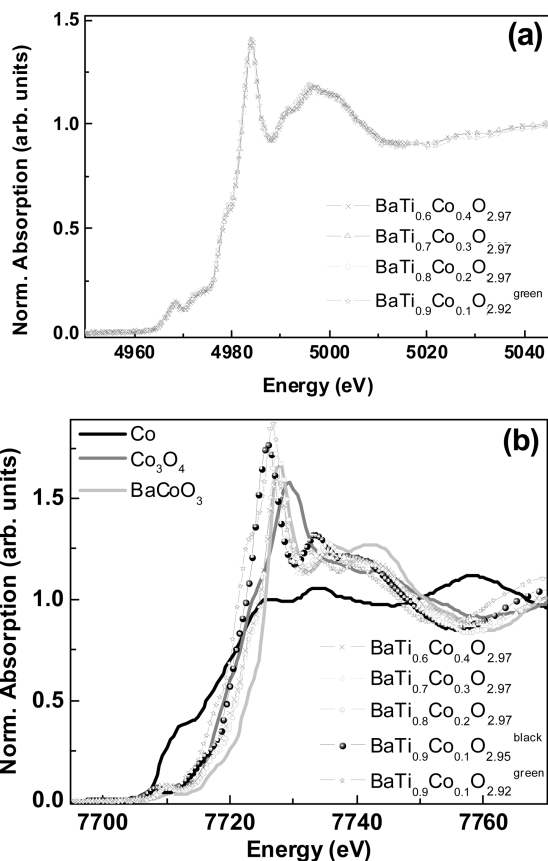

Figure 6. (a) Ti K-edge and (b) Co K-edge XANES spectra of the BaTi$_{1-y}$-Co$_y$O$_{3-\delta}$ samples; several Co K-edge references have been added for comparison.

performed. Ti K-edge and Co K-edge XANES spectra (shown in Figure 6) were collected to establish the oxidation state(s) of the Ti/Co cations. The Ti K-edge spectra (Figure 6a) are all similar and show the same features as that corresponding to BaTiO$_3$,[12,13] therefore confirming only Ti^{4+} ions are present in these samples. On the contrary, slight differences in the shape of the Co K-edge XANES spectra can be observed (Figure 6b). There is higher white-line intensity and a subtle increase in the pre-edge

(13) Moreira, M. L.; Mambrini, G. P.; Volanti, D. P.; Leite, E. R.; Orlandi, M. O.; Pizani, P. S.; Mastelaro, V. R.; Paiva-Santos, C. O.; Longo, E.; Varela, J. A. *Chem. Mater.* **2008**, *20*, 5381.
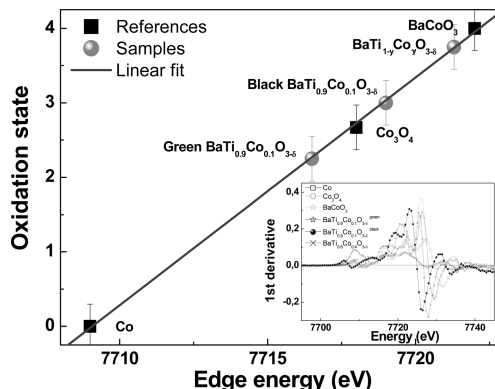

Figure 7. Oxidation state of the BaTi$_{1-y}$Co$_y$O$_{3-\delta}$ samples estimated from the edge position; inset: first derivative curves of the XANES spectra of the BaTi$_{1-y}$Co$_y$O$_{3-\delta}$ series and references.

peak compared to the BaCoO$_3$ spectrum which is used as a reference; this effect becomes more significant as the Co content decreases.

To estimate the Co oxidation state in the samples, the Co K-edge position has been determined from the maxima of the first derivative (Figure 7). For this purpose Co, Co$_3$O$_4$, and BaCoO$_3$ have been used as references. For a Co content between $0.2 \leq y \leq 0.4$, the obtained energy values are similar giving an average oxidation state of Co$^{3.75+}$ that could correspond to a Co^{III}/Co^{IV} ratio close to 20:80 and $\delta \sim 0.02-0.03$. For $y = 0.1$ samples, both green- and black-BaTi$_{0.9}$Co$_{0.1}$O$_{3-\delta}$, the Co K-edge spectra are shifted to lower energy indicating a decrease in the Co oxidation state (average values of $+3$ and $+2.3$ for the black and green phases, respectively).

To confirm the above results, Co K-edges have been fitted by considering different contributions from each oxidation state. Two step functions (error functions, erf(x)) were used to simulate the jumps of Co^{III} and Co^{IV} edges. Moreover, Gaussian functions have been added to reproduce the spectral features, coming from transitions in the absorption process to *4p* states as well as to *3d* states likely hybridized to other *p* levels. To determine an adequate step function for the Co^{4+} contribution, fitting of the BaCoO$_3$ XANES spectra was performed (Figure 8a). Then, another step function was added in the BaTi$_{1-y}$-Co$_y$O$_{3-\delta}$ samples ($y = 0.2, 0.3$, and 0.4) to account for the possible contribution of Co^{3+} ions, Figure 8b.

Finally, for $y = 0.1$ (Figure 8c), spectra for the black BaTi$_{0.9}$Co$_{0.1}$O$_{2.95}$ sample was fitted using only one step function accounting for Co^{3+}, whereas for that corresponding to the green sample, two step functions were included to account for contributions from both Co^{2+} and Co^{3+}, Figure 8d.

The results obtained from the fitting of the XANES spectra are listed in Table 3. All results are in good agreement with the average Co oxidation state estimated previously from the Co K-edge energy value. The Co cations adopt different oxidation states, whereas Ti is present only as Ti^{4+} in 6H-BaTi$_{1-y}$Co$_y$O$_{3-\delta}$ ($0.1 \leq y \leq 0.4$) solid solution. For $0.2 \leq y \leq 0.4$, an average Co$^{3.75+}$ oxidation state is obtained, corresponding to a Co^{3+}: Co^{4+} ratio of 20:80. For $y = 0.1$ all the Co is in the III
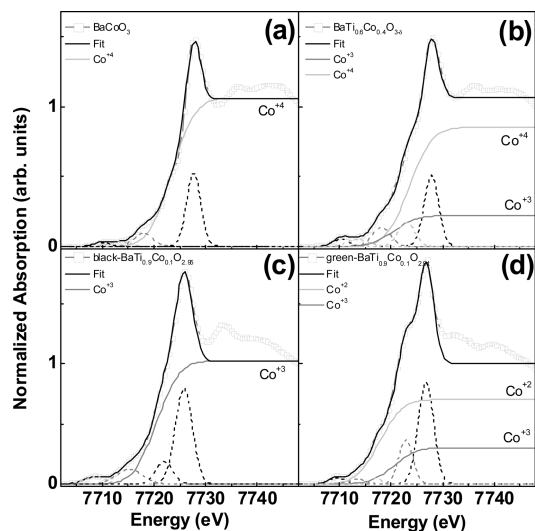
Figure 8. Experimental Co K-edge XANES spectra of (a) $BaCoO_3$, (b) $BaTi_{0.6}Co_{0.4}O_{2.97}$, (c) black-$BaTi_{0.9}Co_{0.1}O_{2.95}$, and (d) green-$BaTi_{0.9}Co_{0.1}O_{2.92}$, and their respective fittings with Co^{2+}, Co^{3+}, and Co^{4+} step functions.

Table 3. Results Obtained from Fitting XANES Spectra for the $6H$-$BaTi_{1-y}Co_yO_{3-\delta}$ System ($y = 0.1, 0.2, 0.3, 0.4$)

y	Co^{II} (%)	Co^{III} (%)	Co^{IV} (%)	oxidation state
0.2−0.4	-	20	80	+3.8
green	70	30		+2.3
black	-	100		+3

oxidation state for the black phase, $BaTi_{0.9}Co_{0.1}O_{2.95}$, whereas Co^{II} and Co^{III} are present in the more reduced, green phase, $BaTi_{0.9}Co_{0.1}O_{2.92}$.

From these results, several conclusions are obtained for the $6H$-$BaTi_{1-y}Co_yO_{3-\delta}$ system. First, there is a solid solution range from $y = 0$ to ~0.4 based on mixed Co^{3+}/Co^{4+} ions for samples prepared in air and, second, it is also possible to form $6H$-$BaTi_{1-y}Co_yO_{3-\delta}$ solid solutions based on mixed Co^{2+}/Co^{3+} ions for samples heat treated under reducing conditions (i.e., $y = 0.1$, green phase). The ability to form $6H$-$BaTiO_3$-type solid solutions where the ratio of the mixed valency associated with the transition metal dopant ion (and therefore oxygen content) is dependent on the preparative conditions, *viz.*, reaction temperature, cooling rate, and oxygen partial pressure has been reported for other systems. For Fe-doped samples,[14] two series of solid solutions with Fe predominantly in the form of Fe^{3+} or Fe^{4+} were prepared by quenching into liquid nitrogen from high temperatures (~1473−1673 K) in air or by slow cooling in flowing O_2 from the reaction temperature down to 473 K, respectively. Similar to the results obtained here for Co-doped samples processed in air, Fe is initially incorporated as Fe^{3+} ions with the formation of O(2) oxygen vacancies, however, the solid solution (under appropriate reaction conditions) can be extended by incorporation of Fe^{4+} ions without the need for additional O(2) oxygen vacancies. The solid solution

(14) Grey, I. E.; Li, C.; Cranswick, L. M. D.; Roth, R. S.; Vanderah, T. A. *J. Solid State Chem.* **1998**, *135*, 312.

ranges are much larger for the Fe system (e.g., ~67% for Fe^{3+}) compared to our Co-doped samples as the end member $BaFeO_{3-\delta}$ can be prepared as a 6H polytype, whereas this is not possible for $BaCoO_{3-\delta}$; it forms either as a 2H- (for $\delta \sim 0$) or 5H-polytype ($\delta \sim 0.2$) depending on the reaction conditions. The difference in polytypism for Fe compared to Co is presumably related to the preference of Co^{4+} ions to occupy face sharing as opposed to corner sharing octahedral environments, e.g., infinite chains of face sharing octahedra along the c-axis in 2H-$BaCoO_3$ or in tetrahedral sites, e.g., in 5H-$BaCoO_{2.8}$ where the oxygen deficiency is ordered and located in c-type layers [c'-BaO_2] to create a 5H stacking sequence of cc'chh based on trimers of face sharing $[Co^{3+/4+}_3O_{12}]$ octahedra linked by corners to two unconnected $[Co^{4+}O_4]$ tetrahedra. A consequence of this difference in bonding preferences results in much smaller solid solution limit(s) for Co^{3+}/Co^{4+} compared to Fe^{3+}/Fe^{4+} in 6H-$BaTiO_3$. The existence of mixed Co^{2+}/Co^{3+} ions in the green phase prepared under reducing conditions suggests that a solid solution volume exists for 6H−$Ba(Ti,Co)O_{3-\delta}$ where the valency of Co can vary from II to IV depending on the preparative conditions.

The variation of cell parameters for the Co-doped samples is shown in Figure 9. For the green phase ($BaTi_{0.9}Co_{0.1}O_{2.92}$, prepared under reducing conditions), there is an increase in **a** and **c** compared to $y = 0$. The increase in **a** is primarily attributed to partial replacement of Ti^{4+} ions by larger Co^{2+} ions, Figure 9 a. The increase in **c** is a consequence of the lower oxygen content of $BaTi_{0.9}Co_{0.1}O_{2.92}$, Figure 9 b. The removal of oxygen atoms from the O(2) sites results in deshielding of the M(2) cations within the dimers; expansion of the cell along the c axis occurs to alleviate the M(2)-M(2) repulsion effects. For the Co^{3+}/Co^{4+} series prepared in air, there is a linear decrease in **a** with increasing y (Figure 9 a), whereas there is an initial increase in **c** between $y = 0$ and 0.1 followed by invariant behavior for $y = 0.2$ to 0.4 (Figure 9 b). The partial substitution of Ti by the smaller Co (III and IV) ions gives rise to the observed decrease in **a**. The **c** parameter is larger for all the Co-doped samples compared to $y = 0$; however, there is no strong dependence on the Co-content. This is correlated with the presence of similar levels of Co^{3+} ions and therefore oxygen vacancies in these samples. Based on the XANES results, the initial increase in **c** from $y = 0$ to 0.1 can be linked to the incorporation of Co as III with the creation of oxygen vacancies. The near invariance of **c** for $y = 0.2$ to 0.4 is linked to the incorporation of Co primarily as IV as opposed to III and therefore does not require any additional oxygen vacancies. The change in slope at $y = 0.1$ for **c** in Figure 9 b therefore indicates a change in substitution mechanism associated with the valence state of the Co-ions for samples prepared in air.

Co and Ti cations are distributed randomly over the various octahedra; however, Ti^{4+} has a strong preference to occupy corner-sharing octahedral sites, as observed also for the $BaMn_{1-y}Ti_yO_{3-\delta}$ system.[7] This feature is more noticeable for lower Co-content samples ($y = 0.1$). The oxygen
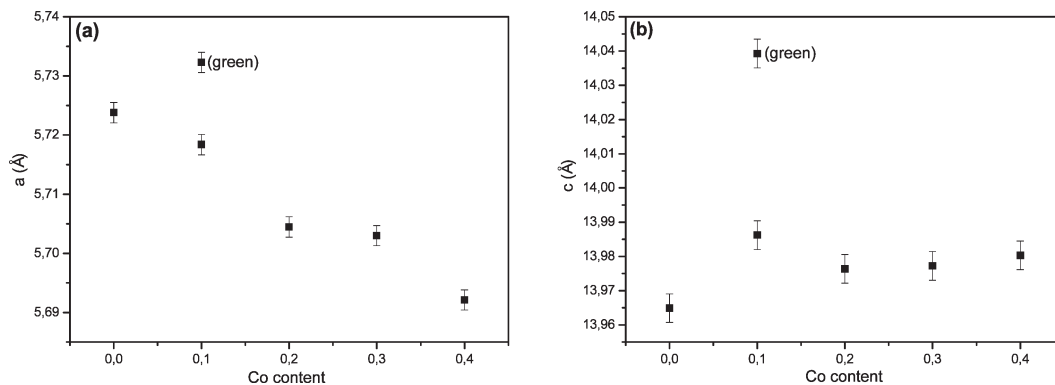
Figure 9. Variation of cell parameters: a (a) and c (b) for BaTi$_{1-y}$Co$_y$O$_{3-\delta}$ samples.

vacancies are located randomly in the hexagonal layers which separate the face sharing octahedra. This is a common feature of many hexagonal polytypes with a nonordered distribution of the oxygen vacancies. For example, in 6H-BaTiO$_{3-\delta}$,[2] BaMnO$_{3-\delta}$,[15] 6H-BaFeO$_{3-\delta}$,[16] 6H′-BaMn$_{1-y}$-Fe$_y$O$_{3-\delta}$,[17] and BaMn$_{1-y}$Ti$_y$O$_{3-\delta}$[7] the oxygen vacancies are accommodated only within the hexagonal layers.

Physical Properties

In view of the diamagnetic state of Ti^{IV} ions a magnetic study was conducted taking into account that Co cations are the only magnetic species present. The temperature dependence of the magnetic susceptibility measured at 1000 Oe is shown in Figure 10. The zero-field-cooled (ZFC) and field-cooled (FC) data are very similar over the measured temperature range. There is no evidence for any magnetic transition so long-range magnetic order is not present in these samples. The magnetic interactions are frustrated by the low concentration of the magnetic Co ions. The susceptibility data show paramagnetic behavior that can be fitted to the Curie−Weiss law from 150 K to RT. All compounds have a negative Weiss temperature (Θ) indicating antiferromagnetic interactions between the magnetic Co ions.

All samples show a lower value of the magnetic moment (∼3.3 μ_B/Co) than the theoretical value ∼5.7 μ_B/Co for y = 0.2−0.4 and ∼4.9 μ_B/Co for y = 0.1, black sample, if we assume Co^{IV} and Co^{III} in high spin configuration. Similar behavior has also been observed for 5H-BaCoO$_{2.80}$ (∼3.9 μ_B/Co) and 12H−Ba$_{0.9}$CoO$_{2.60}$ (∼3.7 μ_B/Co) polytypes. The magnetic moment obtained for the green phase (BaTi$_{0.9}$Co$_{0.1}$O$_{2.92}$) shows an anomalous value. Structural characterization by XRD or XANES does not show the presence of any impurity; therefore, further characterization of this sample is in progress.

Impedance Spectroscopy (IS) and fixed frequency capacitance and dielectric loss measurements were performed on all four samples. Room temperature (RT) measurements
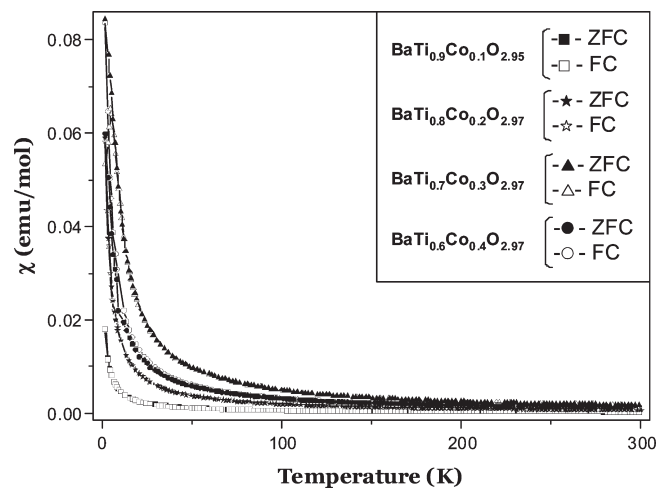
(15) Adkin, J. J.; Hayward, M. A. *Chem. Mater.* **2007**, *19*, 755.
(16) Jacobson, A. J. *Acta Crystallogr., Sect. B: Struct. Sci.* **1976**, *32*, 1087.
(17) Miranda, L.; Sinclair, D. C.; Hernando, M.; Varela, A.; Wattiaux, A.; Boulahya., K.; González-Calbet, J. M.; Parras, M. *Chem. Mater.* **2009**, *21*, 5272.

Figure 10. DC magnetic susceptibility versus temperature under an applied magnetic field of 1 kOe for BaTi$_{1-y}$Co$_y$O$_{3-\delta}$ samples.

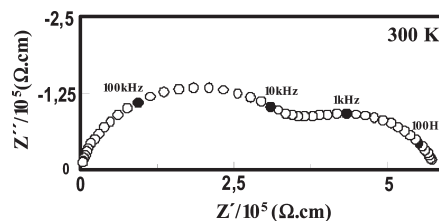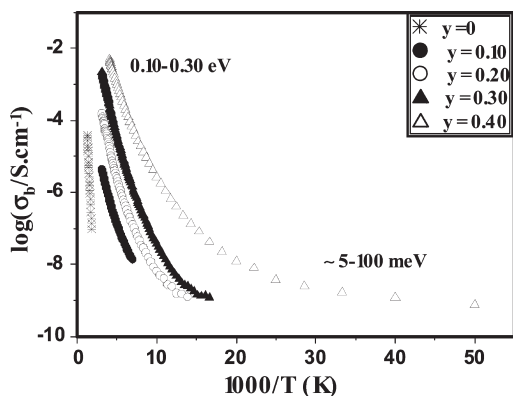**Figure 11.** Z^* plot at 300 K for BaTi$_{0.9}$Co$_{0.1}$O$_{2.95}$.

show the ceramics to be semiconducting, and therefore subambient measurements were required to obtain meaningful data.

Impedance (Z^*) complex plane plots for all samples consisted of two arcs; Figure 11 shows typical data for BaTi$_{0.9}$Co$_{0.1}$O$_{2.95}$ at 300 K. Plots for the other samples are given in Figure 5 of the Supporting Information. IS data could be modeled as a first approximation on an equivalent circuit consisting on two parallel Resistance-Capacitance (RC) elements connected in series. Based on the brickwork model for electroceramics, the higher frequency element, with a lower capacitance value, corresponds to the bulk (intragranular) response, and the lower frequency contribution, with a higher capacitance, corresponds to the grain boundary response. Hence, bulk resistance (corrected for sample geometry), R_b, values were obtained from the

Figure 12. Arrhenius plot of bulk conductivity for $BaTi_{1-y}Co_yO_{3-\delta}$ samples.

intercept of the high frequency arc on the real, Z', axis, and the bulk conductivity, $\sigma_b = 1/R_b$.[18,19]

Arrhenius plots of σ_b for all samples measured in air are shown in Figure 12; for reference, $6H$-$BaTiO_3$ is also included in the plot. σ_b is significantly higher for the Co-doped samples, and the much steeper slope associated with the data for the undoped sample shows the conduction mechanism to be different for the undoped sample compared to the Co-doped samples. There is a clear trend of increasing σ_b with increasing Co-content and for σ_b to deviate from Arrhenius-type linearity at low temperature, especially for $y = 0.4$. Activation energies, E_a, were extracted from the high and low temperature data for the Co-doped samples. E_a was ~0.10 to 0.30 eV for the high temperature data and ~5−100 meV for the low temperature data. This demonstrates that a change in the transport mechanism takes place at low temperature in the Co-doped samples.

Figure 13 shows isothermal $\log\sigma_b$ vs y plots at different temperatures. From RT to ~200 K the isothermal σ_b plots show the same linear trend as a function of Co-content with σ_b increasing by ~4 orders of magnitude for $y = 0.4$ compared to $y = 0.1$. The deviations from linearity that start to occur for data at temperatures < 200 K is related to the change in conduction mechanism that occurs at lower temperature.

The curvature in the Arrhenius plots depicted for all the Co-doped samples at low temperature has been observed in other compounds such as $5H$-$BaMn_{0.2}Co_{0.8}O_{2.80}$,[20] $La_{2-y}Sr_yCu_{1-x}Li_xO_{4-\delta}$,[21] $La_{2-x}Sr_xCuO_{4-\delta}$,[22] $Ba_3MRu_2O_9$,[23] $AA'CoRuO_6$ (A, A'= Sr, Ba, La),[24] and $(R_{1.5}Ce_{0.5})Sr_2$-Cu_2NbO_{10}, R = Pr, Nd, Sm, Eu.[25] This effect may be

(18) Irvine, J. T. S.; Sinclair, D. C.; West, A. R. *Adv. Mater.* **1990**, *2*, 132.
(19) West, A. R.; Sinclair, D. C.; Hirose, N. *J. Electroceram.* **1997**, *1:1*, 65.
(20) Miranda, L.; Feteira, A.; Sinclair, D. C.; García-Hernández, M.; Boulahya, K.; Hernando, M.; Varela, A.; Ramírez, J.; González-Calbet, J. M.; Parras, M. *Chem. Mater.* **2008**, *20*, 2818.
(21) Kastner, M. A.; Birgeneau, R. J.; Chen, C. Y.; Chiang, Y. M.; Gabbe, D. R.; Jenssen, H. P.; Junk, T.; Peters, C. J.; Picone, P. J.; Thio, T.; Thurston, T. R.; Tuller, H. L. *Phys. Rev. B* **1988**, *37*, 111.
(22) Rosseinsky, M. J.; Prassides, K.; Day, P. *J. Mater. Chem.* **1991**, *1*, 597.
(23) Rijssenbeek, J. T.; Matl, P.; Batlogg, B.; Ong, N. P.; Cava, R. J. *Phys. Rev. B* **1998**, *58*, 10315.
(24) Kim, S. H.; Battle, P. D. *J. Solid State Chem.* **1995**, *114*, 174.
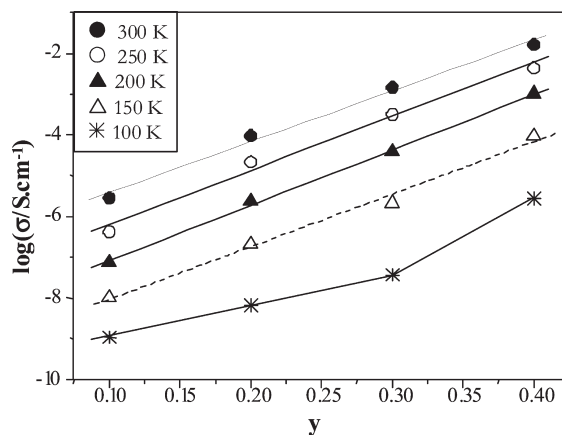(25) Goodwin, T. J.; Radousky, H. B.; Shelton, R. N. *Phys. C* **1992**, *204*, 212.

Figure 13. Isothermal plots of bulk resistivity versus y for $BaTi_{1-y}Co_yO_{3-\delta}$ samples.

associated with thermally activated conductivity based on variable range hopping (VRH). VRH resistivity can be fitted to the following temperature dependence[26]

$$\rho = \rho_0(T)\exp([(T_0/T)^x], \text{where} 0 < x < 1$$

where $x = 1/4$ for the Mott (M-VRH) mechanism for noninteracting electrons or $x = 1/2$ for the Efros-Shklovskii mechanism that includes electron−electron Coulomb interactions. $\rho_0 = AT^{2x}$ is the prefactor and T_0 is the VRH characteristic temperature, where A and T_0 are independent of temperature. The x value is dependent on the density of states so that

$$g(\varepsilon) = N_0\varepsilon^p$$

$$x = (p+1)/(p+4)$$

x can be obtained from the temperature dependence of the conductivity and can therefore be used to obtain p. This equation has physical sense only for $1/4 \leq x \leq 1/2$ and includes the Mott cases for $x = 1/4$ and $1/3$. The different x values give the dependence of the resistivity with temperature and therefore the density of states (DOS) near the Fermi level. As a first approximation, it is enough to establish the relation $\log\rho$ vs T^x, $x = -1$, $-1/2$, $-1/3$, and $-1/4$, without taking into account the pre-exponential factor of E-S.

The variation of bulk resistivity with x for $y = 0.4$ is shown in Figure 14. None of the plots show linear fitting over the entire temperature range measured; however, a larger range of linear fitting is apparent at low temperatures for $x = -1/3$ and $-1/4$. This precludes any conclusion about the exact dimensionality of the conduction mechanism. In general, for such standard Mott plots of conductivity, $x = -1/4$ and $-1/3$ correspond to three- and two-dimensional conductivity (for a constant density of states), respectively. This has been observed in other semiconducting hexagonal perovskites such as oxygen-deficient $6H$-$BaTiO_{2.83}$.[11]

For $y = 0.2$ to 0.4 the oxygen content remains similar $2.97(1)$. Assuming all Ti is present as Ti^{4+}, the Co^{3+}

(26) Shklovskii, B. I.; Efros, A. L. *Electronic properties of semiconductors*; Solid State Science 45, Springer-Verlag: Berlin, 1984.

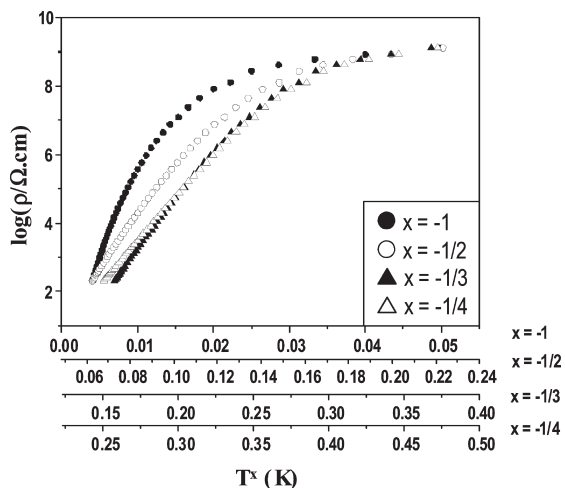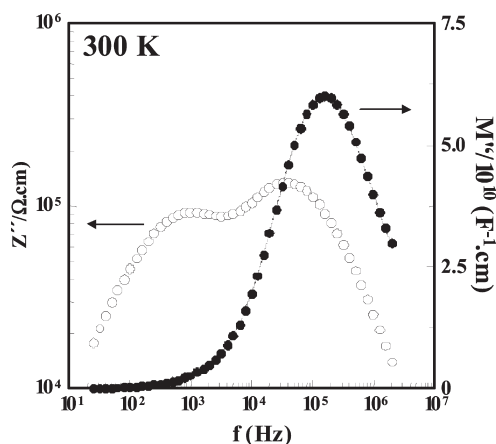**Figure 14.** $\log \sigma_b$ versus T^x of $y = 0.4$ for $x = -1/4, -1/3, -1/2,$ and -1.

Figure 15. Combined, Z'', M'' spectroscopic plot at 300 K for $y = 0.1$.

Figure 16. Fixed frequency (10 kHz) permittivity versus temperature for (a) undoped 6H-BaTiO$_3$, (b) BaTi$_{1-y}$Co$_y$O$_{3-\delta}$ series, and (c) an expanded scale of (b).

content remains approximately constant at ~0.06 and therefore the amount of Co^{4+} increases from 0.14 for $y = 0.2$ to 0.36 for $y = 0.4$ based on a general formula BaTi$^{4+}_{1-y}$(Co$^{3+}_{0.06}$Co$^{4+}_{y-0.06}$)O$_{2.97}$. Given the low values of E_a associated with σ_b, ionic conduction by oxygen vacancies is unlikely and therefore σ_b can be attributed to electronic conduction. The conduction mechanisms at high and low temperatures remain unclear; however, σ_b shows a dramatic increase with the Co^{4+} (d^5) content as opposed to the ratio of Co^{3+}/Co^{4+}. The presence of unpaired electrons on the Co^{4+} ions therefore plays an important role in the conduction mechanism. In addition to the strong overlap of d-orbitals between the M(2) ions within the dimers, the reduction in **a** unit cell parameter with increasing y, Figure 9 a, may improve the orbital overlap between the M(1) and M(2) sites and this may increase the dimensionality of the conduction process associated with the Co-ions.

A more detailed analysis of the IS data for all samples (see Z^* plots in Figure 11 and in Figure 5 of the Supporting Information) reveals the high frequency arc to be nonideal. A combined Z'' and M'' spectroscopic plot for BaTi$_{0.9}$Co$_{0.1}$O$_{3-\delta}$ ceramic at 300 K is shown in Figure 15. (Plots for $y = 0.2$ to 0.4 are given in Figure 6 of the Supporting Information.) The M'' spectroscopic plot shows
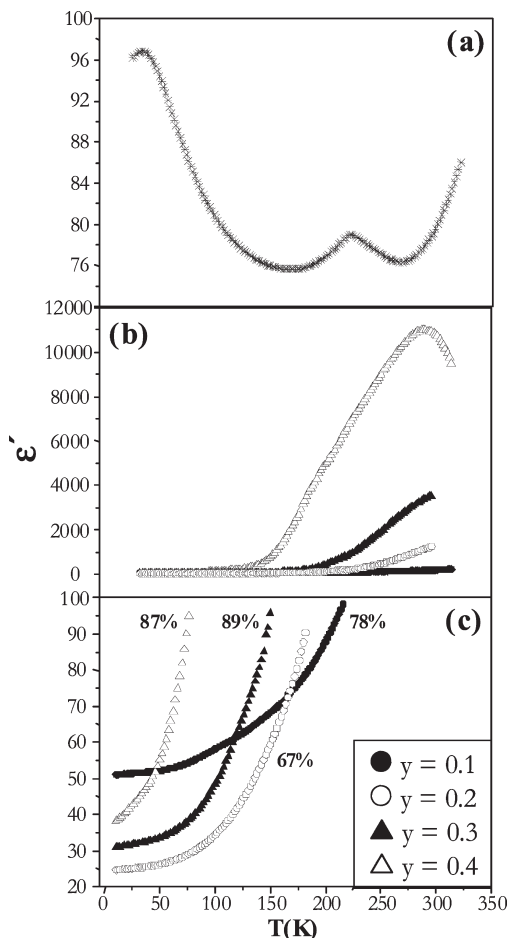
the bulk response to be a non ideal Debye-peak: the half height peak width exceeds the ideal value of 1.14 decades on a logf scale. The nonideal response and therefore electrical heterogeneity associated with the bulk component may arise due to the development of oxygen concentration gradients within the grains. This is more likely to exist when transition metals can exhibit different oxidation states as in the case of 5H-BaMn$_{0.2}$Co$_{0.8}$O$_{2.80}$.[17] The disorder associated with those gradients may be responsible for the change in conduction mechanism observed at low temperatures. Anderson localization of σ_b may therefore occur at low temperatures.

The influence of the Co-content on the permittivity behavior of 6H-BaTiO$_3$ has also been studied by fixed frequency capacitance measurements. Figure 16 shows 10 kHz data for all samples (b and c) and also includes data for undoped 6H-BaTiO$_3$ (a). The clear peaks in the permittivity data for undoped 6H-BaTiO$_3$ correlate well with the subambient polymorphic phase transitions that are known to occur in undoped 6H-BaTiO$_3$ (Figure 16 a). Unfortunately, due to the leaky nature of the Co-doped samples the permittivity data are dominated by space charge polarization for most of the measured temperature range. This explains the very large apparent permittivity values (> 1000) for the Co-doped samples, Figure 16 (b).

The low temperature permittivity data shown in Figure 16 (c) provide the best estimate of the bulk relative permittivity of the samples due to the suppression of the space charge polarization mechanism in this range. The values are in the range of ~20-50 and are in close agreement with those obtained from calculations based on the Clausius-Mossotti equation, e.g. ~63 for $y = 0.1$ and decreasing to ~36 for $y = 0.4$. In general, and as also observed for the 6H-BaMn$_{1-y}$Ti$_y$O$_{3-\delta}$ system,[7] substitution of Ti by a less polarizable cation such as Mn or Co results in a decrease in bulk permittivity for BaTiO$_3$-based materials.

Conclusions

In conclusion, Co is an effective B-site dopant to transform 3C-type BaTiO$_3$ into 6H-type BaTiO$_3$. For BaTi$_{1-y}$Co$_y$O$_{3-\delta}$ samples ($0.1 \leq y \leq 0.4$) prepared in air, δ was established by a combination of hydrogen reduction TGA, ND, and XANES and in all cases $\delta \leq 0.05$. For $y = 0.1$, Co acts primarily as an acceptor dopant and is incorporated as Co^{3+} ions with charge balance achieved by the creation of O(2) site oxygen vacancies. The occurrence of oxygen vacancies ($\delta \sim 0.05$) in $y = 0.1$ is proposed as the driving force for the change in room temperature polymorphism from the 3C- to 6H-polytype similar to that observed for oxygen-deficient, undoped BaTiO$_{3-\delta}$.[10] For samples with $y > 0.1$, Co is present as both Co^{3+} and Co^{4+} ions, and in all cases δ is close to 0.03. This indicates a change from primarily aliovalent (Co^{3+}) to isovalent (Co^{4+}) doping with increasing Co-content with a general formula of BaTi$^{4+}_{1-y}$(Co$^{3+}_{0.06}$Co$^{4+}_{y-0.06}$)O$_{2.97}$ for $0.2 \leq y \leq 0.4$.

XANES data on $y = 0.1$ after heat treatment under reducing conditions revealed the existence mixed state Co^{2+} and Co^{3+} ions that suggests a solid solution volume exists for 6H-Ba(Ti,Co)O$_{3-\delta}$ where the oxidation state of Co can vary from II to IV depending on the preparative conditions.

BaTi$_{1-y}$Co$_y$O$_{3-\delta}$ samples ($0.1 \leq y \leq 0.4$) prepared in air are leaky semiconductors with permittivity in the range ~20−50. The conduction mechanism(s) are complex, but the bulk conductivity is linked to the Co^{4+} content. They all show paramagnetic behavior that can be fitted to the Curie−Weiss law from 150 K to RT with a negative Weiss temperature indicating antiferromagnetic interactions between the magnetic Co ions.

Supporting Information Available: Table I and Figures 1-6. This material is available free of charge via the Internet at http://pubs.acs.org.